Finite Element Modeling for Extracellular Stimulation

Frank Rattay, Simon M. Danner, Ursula S. Hofstoetter and Karen Minassian

Post-print; definite version published in: D. Jaeger and R. Jung (eds.) Encyclopedia of Computational Neuroscience. Springer, New York. 2014. DOI: 10.1007/978-1-4614-7320-6_593-5

Definition

Finite element modeling is an important computational tool in neural engineering to simulate neural excitation with implanted electrodes or with surface electrodes. Besides its importance for analyzing artificially generated neural activities, e.g., in the spinal cord (Danner et al., *2014*; Hofstoetter et al., *2014*), this technique is useful to interpret recorded electrical biosignals generated by neural or muscle tissue activities.

Detailed Description

Neural signals propagate as transmembrane voltage along neural structures, and thereby they cause plenty of tiny currents in any active region of the nervous system. Our understanding of neural activity by means of electrode recordings, e.g., at the surfaces of the skull (EEG), the cortex (ECoG), or intracortically with microelectrodes, is supported by modeling studies that take care of the electrical properties of the biological tissue. Important elements for such studies are the transmembrane currents which act as spatially distributed current sources, the conducting volume, and its electrical properties (Wolters et al. *2006*; Zhang et al. *2006*).

Extracellular electrical stimulation of the neural tissue is another important field of computational neurosciences with increasing impact in neurophysiology, neural engineering, and clinical applications (Rattay *1999*; Rattay et al. *2000*, *2001*; Kunzel and Grill *2004*; Oozeer et al. *2005*; Butson et al. *2007*; Ahuja et al. *2008*; Stickler et al. *2009*; Ladenbauer et al. *2010*; Mou et al. *2012*; Lai et al. *2012*). A third field of interest in finite element modeling (FEM) of volume conductors is the ephaptic coupling of neural structures, that is, the influence of active membranes on the excitability of neighbored cells (Jönsson et al. *2008*; Anastassiou et al. *2010*).

The calculation of the electrical potential Φ in the volume conductor is based on a reduced form of Maxwell's equation, which reads as

$$\nabla \cdot \left(\sigma \nabla \Phi + \epsilon \nabla \frac{\partial \Phi}{\partial t} \right) = 0 \quad (1)$$

where σ is the conductivity and ϵ is the permittivity of the medium. In many applications, neural activities are simulated with compartment models where the transmembrane voltage V is the difference between intra- and extracellular potential, that is, $V = V_i - V_e$. Usually V is calculated with a set

of differential equations of Hodgkin-Huxley type (McNeal *1976*; Rattay *1990*; Mainen et al. *1995*; Rattay et al. *2002*; Kuhn et al. *2009*; Hu et al. *2009*).

External Neuronal Stimulation

Most stimulation modeling studies neglect the secondary influence of the transmembrane currents of excited structures on the electrical field generated by the stimulating electrodes. For more accurate modeling see, e.g., Altman and Plonsey (*1990*) or Martinek et al. (*2008*). In the first modeling step, the excitable structures are not involved, and the electrical field is calculated with FEM or, for simple geometries, with analytical methods. During stimulation, e.g., the application of square pulses, electrode potentials are the driving elements. As intracellular current flow is not included in this first step, Φ is replaced by the extracellular potential V_e in Eq. 1:

$$\nabla \cdot \left(\sigma \nabla V_e + \epsilon \nabla \frac{\partial V_e}{\partial t} \right) = 0 \qquad (2)$$

In order to reduce the computational effort, the minor contribution of the second term in Eq. 2 is often ignored resulting in the quasistatic approach with $\epsilon = 0$. However, investigations of forearm stimulation demonstrated the importance to incorporate tissue capacitance for voltage-regulated transcutaneous stimulation. As consequence of the high skin capacitance, the extracellular potential at the nerve significantly dropped during the applied course of the pulse (Kuhn et al. *2009*). In cases of implanted electrodes, the quasistatic approach deviated less than 6% in comparison with the full solution of Eq. 2. Nevertheless, the electrode tissue interface may cause quite different voltage profiles for current- or voltage-controlled stimulation (Miocinovic et al. *2009*; Goo et al. *2011*).

Second Spatial Derivative of V_e and Current Density Are Used to Predict Regions of Spike Initiation

The goal of many volume conductor studies is the analysis of stimulus-recruitment relations. A common question, e.g., in deep brain stimulation, is as follows: What is the volume of neural tissue activated? The key point of this section is how the FEM output in the region of interest can be used in the second evaluation step for a recruitment analysis of the stimulated tissue. Several criteria are discussed in the following.

Current density criterion. A simple answer for step two comes from the Hodgkin-Huxley formulation where transmembrane currents are computed for 1 cm^2 of the axon membrane, and, consequently, the physical unit of the stimulus is also current density. With this fact in mind, one can assume that spike initiation occurs within a volume around the electrode where current density exceeds a threshold value. In an infinite homogeneous medium, a

monopolar spherical electrode causes current densities proportional to $1/r^2$, where r is the distance from the center of the electrode to the point of interest. In other words, in this simplest approach, spike initiation at distance r demands for electrode currents proportional to r^2. Interestingly, a quite linear relationship between electrical conductivity data and data from diffusion tensor MRI (DTI) of human brain regions (Tuch et al. *2001*) demonstrated essential variations in the direction-dependent conductivity. This relationship allows an improvement in simulating the activated volumes in comparison with the spherical borders of the simplest approach. Thus, the borders of activation can be replaced by patient-specific surfaces based on FEM that combine the body and electrode geometry data with DTI (Butson et al. *2007*).

The morphometric and electrical cell data is often disregarded in FEM analysis due to the variety in tissue shapes and other details not available in the living human brain, and this is a great limitation. From extraneural peripheral nerve stimulation, it is known that thick fibers are recruited easier than thinner ones. This phenomenon is called reverse recruitment order as it reverses the natural recruitment sequence (Blair and Erlanger *1933*). This phenomenon is an example that demonstrates the weakness of simple approaches, which ignores all the electrical properties of nerve cells but uses current density or any other parameter of the volume conductor as recruitment criterion.

Threshold voltage criteria. Several of the early FEM studies published the potential distribution in the body part of interest when stimulated with surface or implanted electrodes. Guided by the threshold voltage hypothesis - an action potential is initiated as soon as the membrane voltage exceeds a value of about 20 mV above the resting state - they had no simple method to define a threshold value for the external potential. Another approach is based on a threshold value for the electrical field (Kasi et al. *2011*). Quite different electrode currents are obviously calculated for the same neural stimulation task depending on the evaluation criteria as the iso-contours of current density, electrical potential, and electrical field are not the same.

Activating Function Criterion

Many modelers prefer a two-step method in order to compute responses of excitable cells to electrical stimulation. In the first step, the electrical field in the volume conductor is calculated. In the second step, a compartment model of a target cell is evaluated. This method is computationally extensive, but it shows the complete spatial and temporal excitation and conduction process of a cell for a given electrode situation. A compartment model is a network of resistances and capacitances, where the current to the center of compartment

n consists of the following components: a capacitive current, ion currents across the membrane, and intracellular currents to neighbored compartments. Current flow in compartment n results in

$$\frac{dV}{dt} = \left[-I_{ion,n} + \frac{V_{n-1}-V_n}{\frac{R_{n-1}}{2}+\frac{R_n}{2}} + \frac{V_{n+1}-V_n}{\frac{R_{n+1}}{2}+\frac{R_n}{2}} + \frac{V_{e,n-1}-V_{e,n}}{\frac{R_{n-1}}{2}+\frac{R_n}{2}} + \frac{V_{e,n+1}-V_{e,n}}{\frac{R_{n+1}}{2}+\frac{R_n}{2}} \right] / C_n \quad (3)$$

with transmembrane potential V, ion current I_{ion} , axial resistance R, and membrane capacity C. The direct stimulating influence of the extracellular potential on compartment n is defined by the activating function f (Rattay *1999*) which is the driving term of the differential Eq. 3:

$$f_n = \left[\frac{V_{e,n-1}-V_{e,n}}{\frac{R_{n-1}}{2}+\frac{R_n}{2}} + \frac{V_{e,n+1}-V_{e,n}}{\frac{R_{n+1}}{2}+\frac{R_n}{2}} \right] / C_n. \quad (4)$$

For a fiber with constant diameter d, constant compartment length Δx, intracellular resistivity r_i, and specific capacity c, Eq. 4 is reduced to

$$f_n = \frac{d}{4c \cdot \rho_i} \cdot \frac{V_{e,n-1}-2V_{e,n}+V_{e,n+1}}{\Delta x^2}. \quad (5)$$

All terms within the brackets of Eqs. 3 and 4 are currents. Therefore, neglecting the weighting factor $1/C$, the stimulating influence of the activating function f can be interpreted as an injected virtual current in every compartment. In regions where this current is positive, the membrane depolarizes, and where it is negative, it tends to hyperpolarize. For the case of a long straight excitable fiber (axon, dendrite, or muscle fiber) with constant diameter, Fig. 1 explains the activating function concept for cathodic stimulation on the basis of virtual current injection. Note that the second term on the right side of Eq. 5 is the second difference quotient of the extracellular potential along the fiber. With $\Delta x \to 0$, f becomes proportional to the second derivative of V_e, and therefore $d^2 V_e/dx^2 > 0$ indicates the regions for spike initiation.

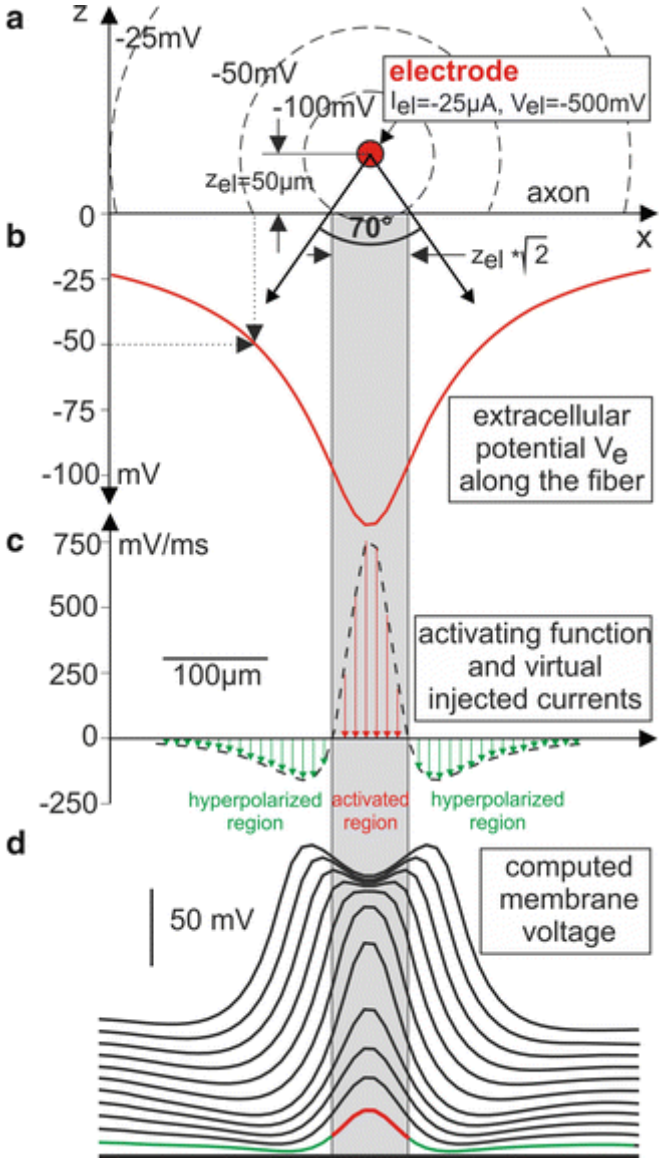

Figure 1. Extracellular stimulation of a straight unmyelinated axon with a small spherical electrode. (**a**) Geometry and isopotentials, simulated for an equivalent point source 50 µm above a fiber positioned at the x-axis. (**b**) Extracellular potential $V_e = \varrho_e I_{el}/4\pi r$ with $r = \mathrm{sqrt}((x-x_{el})^2+z_{el}^2)$ is used to calculate the activating function. (**c**) A fiber with $d = 1$ µm and compartment length $\Delta x = 10$ µm results in a peak activating function value of 740 mV/ms. According to Eq. 5, this is the slope of the membrane voltage in the compartment below the electrode at the beginning of the −25 µA pulse. According to Eq. 4, the virtual currents are $f_n C_n$. With $C_n = d\pi\Delta x c = 3.14159*10^{-7}$ µF/cm^2 and specific membrane capacity $c = 1$ µF/cm^2, the maximum injected current is 232 pA at the center of the activated region. As the length of the activated region ($1.414*z_{el}$) is defined by an angle of 70° (Rattay *1986*), this region increases in a linear way with the electrode distance. (**d**) Vertically shifted transmembrane voltage profiles in time steps of 200 µs. The first response of the neuron at the beginning of the stimulus pulse is proportional to the activating function shown in *C*: hyperpolarized and depolarized regions in *green* and *red*, respectively.

We assume that the axon is at rest before a stimulus is applied (Fig. 2). During this resting phase, the sum of the first three terms at the right side of Eq. 3 is zero, and consequently the activating function quantifies the slope of membrane voltage at stimulus onset in every compartment. The activating function is the rate of transmembrane voltage change and it has the unit mV/ms. Note that the activating function predicts the reverse recruitment order phenomenon as the scaling factor of f is proportional to fiber diameter d (Eq. 5).

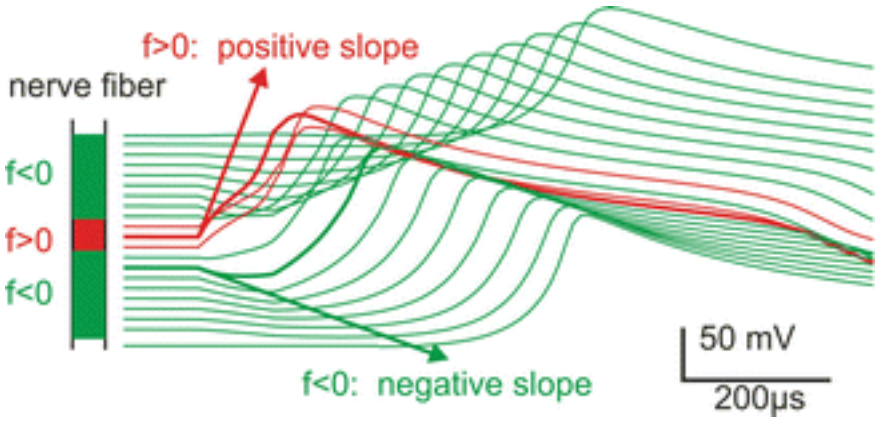

Figure 2. Hyperpolarized (*green*) and depolarized (*red*) regions of a stimulated axon (*left*) and voltage profiles as functions of time for the compartment model shown in Fig. 1 (*right*). Every *line* shows the transmembrane voltage of a compartment as function of time with a vertical shift according to the position of the compartment. The axon is for 100 µs in the resting state before it is stimulated with a cathodic 100 µs pulse as in Fig. 1d. The compartment closest to the cathodic electrode has the largest activating function value, and it is the spike initiation site (*thick red line*). As predicted by Fig. 1c, the largest slope in the *red* region ($f > 0$) is about four times the value of the largest *green* slope indicated by the *green arrow*. Therefore, a change of stimulus polarity needs about four times larger electrode threshold currents. This theoretical result for extracellular axon stimulation (Rattay *1986*) is in accordance with experimental observations (Ranck *1975*).

Stimulus Threshold Current Depends Also on Type and Densities of Ion Channels

The activating function concept is an essentially better predictor for spike initiation than all the other methods presented at the beginning of the last section. The activating function is a fascinating concept because of its simplicity to predict regions of excitation in a target neuron without using knowledge about the ion channel compositions of the excitable membranes. However, simulating the gating processes of the cell membrane is needed for further improvements of cell response prediction.

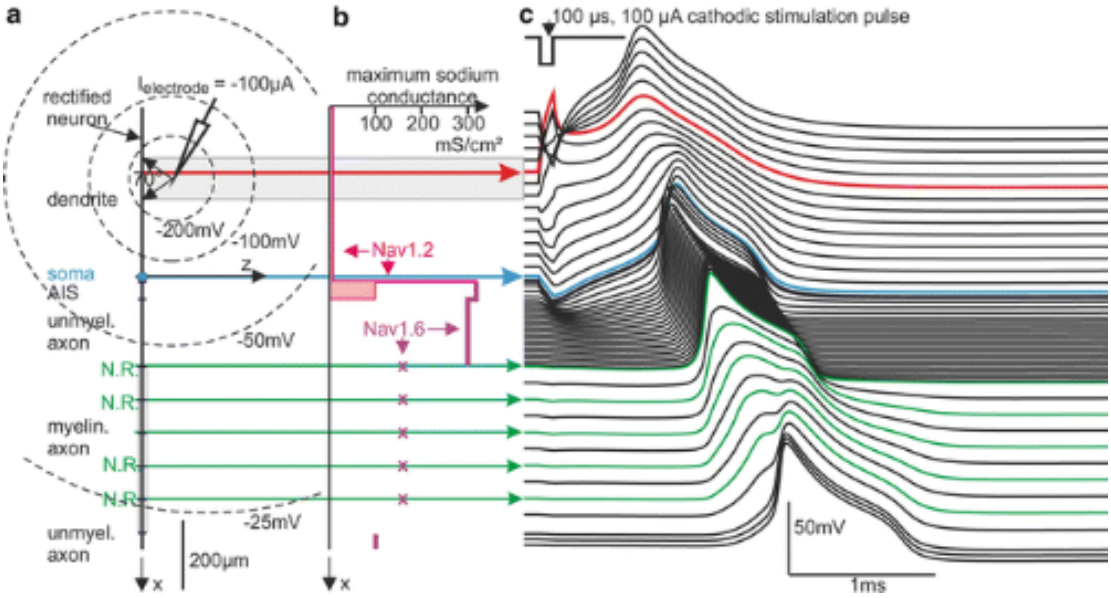

Figure 3. Cathodic microelectrode stimulation at the dendrite of a rectified pyramidal cell. (**a**) The non-branching model cell consists of the following functionally different segments: dendrite, soma, axon initial segment (*AIS*), unmyelinated axon, myelinated axon with active membranes in the nodes of Ranvier (*NR*), and an unmyelinated terminal. (**b**) Two types of sodium channels enable initiation and conduction of spikes. High-threshold Nav1.2 channel densities represented by the maximum conductance (*magenta*) exist in the upper part of the neuron until AIS and low-threshold Nav1.6 channels (*purple*) from AIS until the axon terminal. Note that high concentrations from axon hillock until myelination exceed even that of nodes of Ranvier by a factor 2, whereas in soma and dendrite, a uniform maximum sodium conductance of 8 mS/cm^2 is assumed (Hu et al. *2009*). (**c**) Transmembrane voltages as functions of time. Electrode tip is assumed 300 µm from the soma and 80 µm from the axis (x_{el} = 300 µm, z_{el} = 80 µm) in a homogeneous medium with resistivity ϱ_e = 300 Ω * cm. At this distance the electrical field has a direct depolarizing effect only within the *gray-shaded* region where the slopes at stimulus onset in (**c**) are positive. Spike is initiated in the compartment closest to the electrode (*red*) and propagates in both directions. When intracellular currents cross the soma (*cyan*), they activate the low-threshold regions in the axon, and therefore action potential peaks appear earlier in these axon compartments than in the soma and the last presomatic dendritic compartments.

The important impact of ion channel compositions in the functionally different segments of a stimulated neuron is demonstrated with the following examples. In order to reduce geometric influences, microelectrode stimulation of a cortical pyramidal cell is simulated by a non-branching rectified model cell. Ion channel gating dynamics and more details about electrical and geometrical data are given in Rattay and Wenger (*2010*). Even the low density of high-threshold sodium channels (Nav1.2) enables a conducted spike to be initiated within the dendrite (Fig. 3). For this electrode position close to the dendrite, the positive values of the activating function are found within a

small region in the dendrite as predicted by the 70° limit shown in Fig. 1. An interesting phenomenon appears when the dendrite is passive or also when the sodium channel density is reduced in the modeled neuron below a critical value needed for action potential conductance. In such cases where the stimulating microelectrode is in front of the soma, the neuron is not excitable with negative pulses. This phenomenon becomes effective for the model assumptions when the electrode-dendrite distance is reduced because current influx within a shortened active zone (defined by the 70° borders, Fig. 1) cannot excite the neighboring hyperpolarized regions. Surprisingly, this failure effect is more pronounced for thicker fibers. This is in contrast to the reverse recruitment order for excitable fibers. For details see Rattay and Wenger (*2010*).

In the next example, the electrode is moved in constant distance along the axis of the neuron. Several phenomena can be observed (Fig. 4a). (i) The distal end of the axonal initial segment with high Nav1.6 channel density is very sensitive to cathodic stimulation, and this is a preferred site of spike initiation. (ii) The neuron is even more excitable at the third and fourth nodes of Ranvier despite the essentially lower ion channel densities. It is a general property that myelinated axons are easier to excite than unmyelinated ones which is a consequence of higher activating function values in nodes of Ranvier that are favored by the properties of the internodes (Rattay *1986*, *1990*, *1999*). (iii) Moving the electrode along the thick dendrite in a distance of 100 μm from the neuron axis needs about twice the threshold current in comparison to the positions along the axon. (iv) The thresholds in 50 μm distance are higher as expected according to the prediction of the quadratic rule proposed in the literature (Stoney et al. *1968*; Tehovnik et al. *2006*; Butson et al. *2007*), shown by dashed blue line in Fig. 4a and by Fig. 4b. (v) Electrodes above the center of an internode need doubled threshold currents compared to positions above a node of Ranvier. This node-internode threshold relation known from peripheral nerve stimulation becomes more and more pronounced when electrode-fiber distance is reduced (Rattay *1987*). (vi) Within a dendritic region (-149 μm $< x_{el} < -37$ μm), anodic threshold is lower than cathodic which is in agreement with experiments (Ranck *1975*) and theory (Rattay *1999*). (vii) Anodic threshold current of the 5 μm diameter dendrite example increases in an exponential way with distance from the soma (comp. the rather linear relation of the left part of the green line in the logarithmic current scaling of Fig. 4a). The thin dendrite has another threshold characteristic as explained below. (viii) The extreme node-internode threshold fluctuations seen for cathodic pulses are lost when pulse polarity is reversed. (ix) In general thin dendrites have higher thresholds (comp. thin and thick green and blue lines in Fig. 4a).

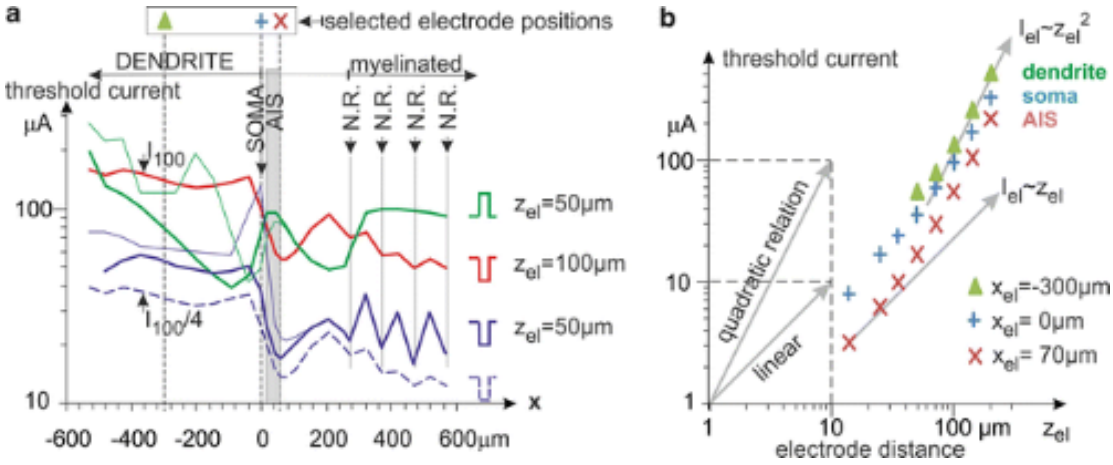

Figure 4 Threshold current as a function of electrode position for monophasic 100 µs pulses for the model neuron of Fig. 3. (**a**) When the microelectrode tip is moved from left to right in constant 100 µm distance to the neuron axis, cathodic threshold current (*red line*, marked as I_{100}) is rather constant along the dendrite, but threshold decreases quickly before arriving at the soma ($x_{el} = 0$) with a local minimum at the distal end of the AIS (AIS is marked as *gray* region). The zigzag line demonstrates low thresholds when the electrode is just above a node of Ranvier. For half the axial distance ($z_{el} = 50$ µm), cathodic threshold (*blue line*) is similar in shape with the broken blue line which is the prediction for a quadratic current distance rule ($I_{100}/4$ is a vertical shift of the *red* I_{100} line, corresponding to the factor 1/4 of the logarithmic scale). However, two discrepancies are characteristic: full *blue line* values are always higher and, second, the threshold ratio for nodal and internodal positions is increased. Anodic stimulation (*green line*) does neither favor positions above nodes nor the vicinity of the AIS. Thin *green* and *blue lines* show threshold predictions when the dendritic diameter is reduced from 5 to 1.25 µm. (**b**) Radial current distance relations for three selected positions as marked in (**a**): middendritic, soma, and distal end of *AIS*. Indicated by the slopes of the *gray* arrows, in all three cases, there is a clear trend from a linear to a quadratic relation when electrode distance is increased in radial direction.

Stimulation of the Lumbar Spinal Cord with Epidural Electrodes

In the following modeling example, we analyzed which neural elements are primarily excited in order to explain observations during human lumbar cord stimulation (Dimitrijevic et al. *1998*; Minassian et al. *2007*, "Paraspinal Magnetic and Transcutaneous Electrical Stimulation" in this encyclopedia). As described above, we used a two-step procedure for this task. In the first step, isopotentials are computed with finite element software ANSYS for a typical position of a bipolar electrode as implanted in paralyzed patients (Fig. 5). The stimulator (Itrel 3, model 7425, Medtronic) delivered continuous, non-patterned stimulation with 1-10 V at 2.2-130 Hz and asymmetric biphasic pulses with a 210 µs main pulse and a long second pulse for avoiding charge accumulation. Because of its overlength, the influence of the second pulse can

be neglected in this quasistatic approach, and all presented conclusions could be done with a single finite element evaluation.

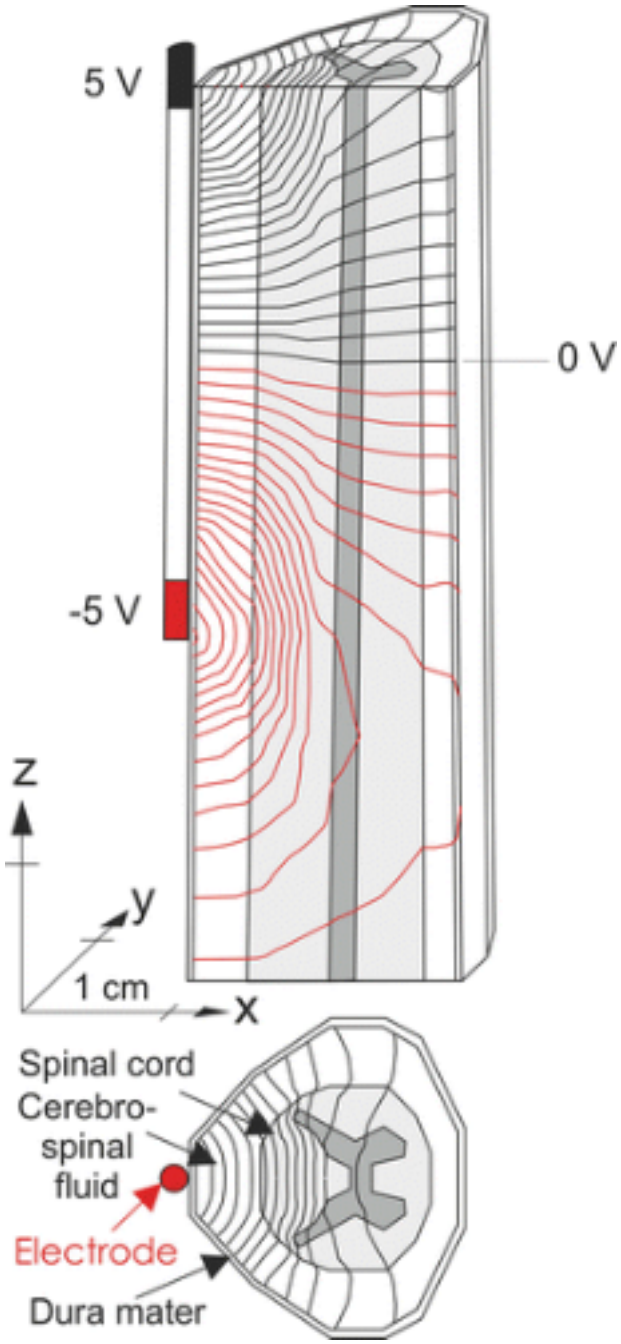

Figure 5. Potential distribution within the dural sac is computed with the finite element method for bipolar stimulation with an implanted electrode. The volume of interest has to be embedded into a larger volume in order to use appropriate boundary conditions, e.g., a cylindrical body segment (not shown, with no current flow components across the surface). Axons close to the cathode (*red potential lines*) are preferred targets for stimulation.

The compartment models of the target neurons are based on the CRRSS (Chiu-Ritchie-Rogart-Stagg-Sweeney) model in the form described in

Rattay (*1990*) and Rattay et al. (*2002*). The resulting differential equations were evaluated with software ACSL. Spike initiation points were also analyzed with the activating function concept.

The purpose of our investigations was to find which neural elements are the primarily excited ones. First ideas are guided by the general knowledge that myelinated fibers are easier to excite than the unmyelinated. Moreover, thick axons have lower thresholds than thin axons, a fact that is deduced from the weighting factor $d/4r_i c$ in Eq. 5. Therefore, the thick sensory afferents may be most sensitive to low stimuli. However, it could be that the thinner dorsal column fibers are even more sensitive as they may be closer to the electrode at the thoracic level. Such fibers are comparable in diameter and position with the vertical branches of our target neuron marked by red arrow in Fig. 6a.

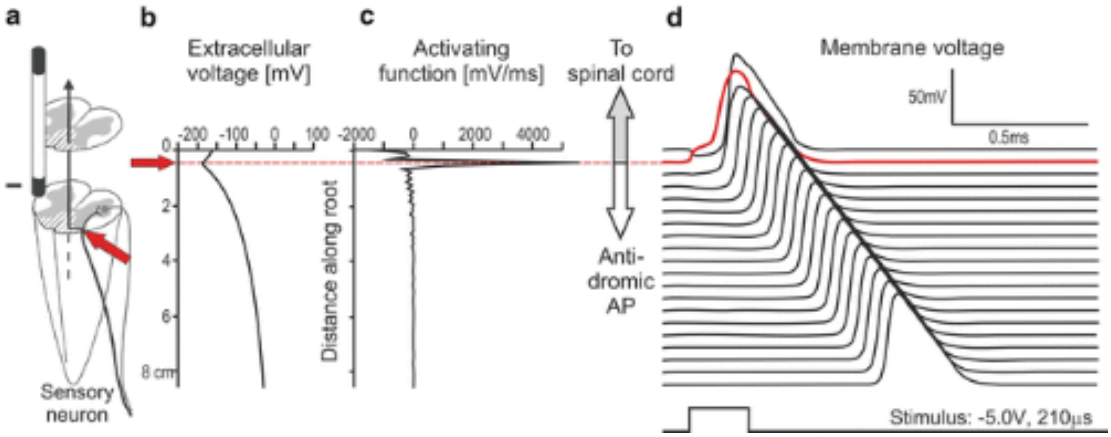

Figure 6. (**a**) Three-dimensional view of the lower spinal cord with a sensory fiber (within the posterior root, curved trajectory) and its axonal branches in the back side of the spinal cord (hatched area, *vertical arrow*) with a single synaptic connection to a motoneuron. *Red arrows* and *red line* indicate the hot spot for the spike initiation at the site where the posterior root fiber enters the spinal cord. (**b**) Extracellular voltage generated by epidural stimulation, (**c**) activating function, and (**d**) membrane voltage for an S1 posterior root fiber stimulated 4 % above the characteristic fiber threshold with a midsagittal electrode at L4 spinal cord level. Note that the positive part of the activating function is restricted to a single node of Ranvier (*peak*). In this hot spot an action potential is generated that propagates into the spinal cord and in antidromic direction.

The activating function concept shows two closely neighbored hot spots in the afferent rootlet fibers: the regions with sharp curvature before the entry point in the spinal cord and the entry point itself where a sudden change of the electrical conductivity at the interface between two media supports the initiation of action potentials. Both cases result in large values of the second spatial derivative of V_e and thus of the activating function. Computer evaluations with the full system of differential equations demonstrated that

with the applied stimulus intensities, spikes can typically be generated in rootlets, which enter the spinal cord up to 2 cm below the level of the cathode, but there is no spike initiation in the dorsal columns in the case of lumbar stimulation.

Other candidates for spike initiation for epidurally placed lumber spinal cord electrodes are the AIS of spinal interneurons and their myelinated axonal segments. A comparison with Fig. 4a shows that AIS excitation has about the same threshold as the nodes of Ranvier. As the axons of the interneurons are essentially thinner than that of the Ia afferents and even thinner than the dorsal column fibers, model interpretation predicts significantly larger thresholds for interneurons than for thick axons in sensory rootlets.

Further details and related explanations are found in Danner et al. (*2014*) and Hofstoetter et al. (*2014*).

Conclusions

Finite element evaluation of the electrical field is an important tool for modeling nerve stimulation. The most important question in this context is which of the FE output data should be used to quantify the recruitment order of the excitable tissue. In this entry, it was shown that current density is not a good indicator, but it is of value for a rough approach if no information is available about geometrical and electrical details of the involved neural structures. Better insights can be found from the activating function concept and from the compartment.

Spatial differences in ion channel compositions within a single neuron can cause surprising phenomena. Such phenomena can be detected when all differential equations of the compartment model of a target neuron are evaluated. On the other hand, some remarkable observations about spike initiation sites are based on geometric configurations that can be explained with FEM. An example is that hot spots in sensory afferents stimulated with implanted epidural lumbar cord electrodes can be the same when transcutaneous stimulation is applied (Ladenbauer et al. *2010*; Danner et al. *2011*, *2014*). The effect is surprising as both the larger distance to the axon and the larger electrode size of the surface electrode suggest a poor focusing effect in comparison with the implanted electrodes.

Another surprising phenomenon, which was recently discovered, is the rather poor focal stimulation success with microelectrodes. Low-current stimulation produces a sparse and distributed set of activated cells often with distances of several hundred micrometers between the cell bodies and the microelectrode (Histed et al. *2009*). A reasonable hypothesis to explain the sparely distributed population of somas results from a computer simulation analysis based on a rather dense concentration of collaterals of many neurons in the close surrounding of the electrode tip. These thin axons and dendrites

are capable of generating an ongoing nerve impulse or activating the distant AIS via intracellular current flow. Therefore, the cell bodies of stimulated cells can be situated within a distance of several hundred micrometers or more relative to the electrode tip, whereas most of the cell bodies closer to the electrode have a small probability to be activated (Rattay and Wenger *2010*). A similar conclusion is reported concerning the spinal cord. Previous studies demonstrated that extracellular stimulation within the spinal cord activates fibers in passage at lower stimulus intensities than neuronal cell bodies (Renshaw *1940*). Action potentials elicited in localized terminal branches of afferents are assumed to spread antidromically to all terminal branches of the afferents and transsynaptically excite motoneurons and interneurons far away from the stimulation site (Gaunt et al. *2006*).

Acknowledgment

We wish to acknowledge the support of the Vienna Science and Technology Fund (WWTF), Proj. Nr. LS11-057.

References

Ahuja AK, Behrend MR, Kuroda M, Humayun MS, Weiland JD (2008) An in vitro model of a retinal prosthesis. IEEE Trans Biomed Eng 55:1744-1753

Altman KW, Plonsey R (1990) Point source nerve bundle stimulation: effects of fiber diameter and depth on simulated excitation. IEEE Trans Biomed Eng 37:688-698

Anastassiou CA, Montgomery SM, Barahona M, Buzsáki G, Koch C (2010) The effect of spatially inhomogeneous extracellular electric fields on neurons. J Neurosci 30:1925-1936

Blair EA, Erlanger J (1933) A comparison of the characteristics of axons through their individual electrical responses. Am J Physiol 106:524-564

Butson CR, Cooper SE, Henderson JM, McIntyre CC (2007) Patient-specific analysis of the volume of tissue activated during deep brain stimulation. Neuroimage 34:661-670

Danner SM, Hofstoetter US, Minassian K (2014) Finite Element Models of Transcutaneous Spinal Cord Stimulation. In: Jaeger D, Jung R (eds) Encyclopedia of Computational Neuroscience. Sprinter, New York, pp 1-6. DOI: 10.1007/978-1-4614-7320-6_604-4

Danner SM, Hofstoetter US, Ladenbauer J, Rattay F, Minassian K (2011) Can the human lumbar posterior columns be stimulated by transcutaneous spinal cord stimulation? A modeling study. Artif Organs 25:257-262

Dimitrijevic MR, Gerasimenko Y, Pinter MM (1998) Evidence for a spinal central pattern generator in humans. Annu NY Acad Sci 860:360-376

Gaunt RA, Prochazka A, Mushahwar VK, Guevremont L, Ellaway PH (2006) Intraspinal microstimulation excites multisegmental sensory afferents at lower stimulus levels than local alpha-motoneuron responses. J Neurophysiol 96:2995-3005

Goo YS, Ye JH, Lee S, Nam Y, Ryu SB, Kim KH (2011) Retinal ganglion cell responses to voltage and current stimulation in wild-type and rd1 mouse retinas. J Neural Eng 8:035003

Hofstoetter US, Danner SM, Minassian K (2014) Paraspinal Magnetic and Transcutaneous Electrical Stimulation. In: Jaeger D, Jung R (eds) Encyclopedia of Computational Neuroscience. Sprinter, New York, pp 1-21. DOI: 10.1007/978-1-4614-7320-6_603-5

Histed MH, Bonin V, Reid RC (2009) Direct activation of sparse, distributed populations of cortical neurons by electrical microstimulation. Neuron 63:508-522

Hu W, Tian C, Li T, Yang M, Hou H, Shu Y (2009) Distinct contributions of Nav1.6 and Nav1.2 in action potential initiation and backpropagation. Nat Neurosci 12:996-1002

Jönsson R, Hanekom T, Hanekom JJ (2008) Initial results from a model of ephaptic excitation in the electrically excited peripheral auditory nervous system. Hear Res 237:49-56

Kasi H, Hasenkamp W, Cosendai G, Bertsch A, Renaud P (2011) Simulation of epiretinal prostheses - evaluation of geometrical factors affecting stimulation thresholds. J Neuroeng Rehabil 8:44

Kuhn A, Keller T, Lawrence M, Morari M (2009) A model for transcutaneous current stimulation: simulations and experiments. Med Biol Eng Comput 47:279-289

Kuncel AM, Grill WM (2004) Selection of stimulus parameters for deep brain stimulation. Clin Neurophysiol 115:2431-2441

Ladenbauer J, Minassian K, Hofstoetter US, Dimitrijevic MR, Rattay F (2010) Stimulation of the human lumbar spinal cord with implanted and surface electrodes: a computer simulation study. IEEE Trans Neural Syst Rehabil Eng 18:637-645

Lai HY, Liao LD, Lin CT, Hsu JH, He X, Chen YY, Chang JY, Chen HF, Tsang S, Shih YY (2012) Design, simulation and experimental validation of a novel flexible neural probe for deep brain stimulation and multichannel recording. J Neural Eng 9:036001

Mainen ZF, Joerges J, Hugenard JR, Sejnowski TJ (1995) A model of spike initiation in neocortical pyramidal neurons. Neuron 15:1427-1439

Martinek J, Stickler Y, Reichel M, Mayr W, Rattay F (2008) A novel approach to simulate Hodgkin-Huxley-like excitation with COMSOL multiphysics. Artif Organs 32:614-619

McNeal DR (1976) Analysis of a model for excitation of myelinated nerve. IEEE Trans Biomed Eng 23:329-337

Minassian K, Persy I, Rattay F, Pinter MM, Kern H, Dimitrijevic MR (2007) Human lumbar cord circuitries can be activated by extrinsic tonic input to generate locomotor-like activity. Hum Mov Sci 26:275-295

Miocinovic S, Lempka SF, Russo GS, Maks CB, Butson CR, Sakaie KE, Vitek JL, McIntyre CC (2009) Experimental and theoretical characterization of the voltage distribution generated by deep brain stimulation. Exp Neurol 216:166-176

Mou Z, Triantis IF, Woods VM, Toumazou C, Nikolic K (2012) A simulation study of the combined thermoelectric extracellular stimulation of the sciatic nerve of the *Xenopus laevis*: the localized transient heat block. IEEE Trans Biomed Eng 59:1758-1769

Oozeer M, Veraart C, Legat V, Delbeke J (2005) Simulation of intra-orbital optic nerve electrical stimulation. Med Biol Eng Comput 43:608-617

Ranck JB (1975) Which elements are excited in electrical stimulation of mammalian central nervous system: a review. Brain Res 98:417-440

Rattay F (1986) Analysis of models for external stimulation of axons. IEEE Trans Biomed Eng 33:974-977

Rattay F (1987) Ways to approximate current-distance relations for electrically stimulated fibers. J Theor Biol 125:339-349

Rattay F (1990) Electrical nerve stimulation: theory, experiments and applications. Springer, New York

Rattay F (1999) The basic mechanism for the electrical stimulation of the nervous system. Neuroscience 89:335-346

Rattay F, Wenger C (2010) Which elements of the mammalian central nervous system are excited by low current stimulation with microelectrodes? Neuroscience 170:399-407

Rattay F, Minassian K, Dimitrijevic MR (2000) Epidural electrical stimulation of posterior structures of the human lumbosacral cord: 2. Quantitative analysis by computer modeling. Spinal Cord 38:473-489

Rattay F, Leao RN, Felix H (2001) A model of the electrically excited human cochlear neuron. II. Influence of the three-dimensional cochlear structure on neural excitability. Hear Res 153:64-79

Rattay F, Greenberg R, Resatz S (2002) Neuron modeling. In: Finn WE, LoPresti PG (eds) Handbook of neuroprosthetic methods. CRC Press, Boca Raton, pp 39-71

Renshaw B (1940) Activity in the simplest spinal reflex pathways. J Neurophysiol 3:373-387

Stickler Y, Martinek J, Rattay F (2009) Modeling needle stimulation of denervated muscle fibers: voltage-distance relations and fiber

polarization effects. IEEE Trans Biomed Eng 56:2396-2403

Stoney SD, Thompson WD, Asanuma H (1968) Excitation of pyramidal tract cells by intracortical microstimulation: effective extent of stimulating current. J Neurophysiol 31:659-669

Tehovnik EJ, Tolias AS, Sultan F, Slocum WM, Logothetis NK (2006) Direct and indirect activation of cortical neurons by electrical microstimulation. J Neurophysiol 96:512-521

Tuch DS, Wedeen VJ, Dale AM, George JS, Belliveau JW (2001) Conductivity tensor mapping of the human brain using diffusion tensor MRI. Proc Natl Acad Sci U S A 98:11697-11701

Wolters CH, Anwander A, Tricoche X, Weinstein D, Koch MA, MacLeod RS (2006) Influence of tissue conductivity anisotropy on EEG/MEG field and return current computation in a realistic head model: a simulation and visualization study using high-resolution finite element modeling. Neuroimage 30:813-826

Zhang Y, Ding L, van Drongelen W, Hecox K, Frim DM, He B (2006) A cortical potential imaging study from simultaneous extra- and intracranial electrical recordings by means of the finite element method. Neuroimage 31:1513-1524